Version of Record: https://www.sciencedirect.com/science/article/pii/S0303243418305440
Manuscript_aa077444d0e95834edde8000091520d1

Fire detection and temperature retrieval using EO-1 Hyperion data over selected Alaskan boreal forest fires

Christine F. Waigl[a,1], Anupma Prakash[a], Martin Stuefer[a], David Verbyla[b], Philip Dennison[c]

[a] *Geophysical Institute, University of Alaska Fairbanks*

[b] *School of Natural Resources and Extension, University of Alaska Fairbanks*

[c] *Geography Department, University of Utah*

Abstract

Infrared imaging spectrometers are used to map and characterize wildland fire based on their sensitivity to fire-emitted thermal radiation and ability to resolve spectral emission or absorption features. There is a general paucity of research on the use of space-borne imaging spectroscopy to study active fires in the North American boreal forest. We used hyperspectral data acquired by the Hyperion sensor on the EO-1 satellite over three wildfires in Alaska's boreal forest to evaluate three fire detection methods: A metric to detect an emission feature from potassium emitted by biomass burning; a continuum-interpolated band ratio (CIBR) that measures the depth of a carbon dioxide absorption line at 2010 nm; and the Hyperspectral Fire Detection Index (HFDI), which is a normalized difference index based on spectral radiance in the short-wave infrared range. We found that a modified version of the HFDI produces a well-defined map of the active fire areas. The CO_2 CIBR, though affected by sensor noise and smoke, contributes a slight improvement to the fire detection performance when combined with HFDI-type indices. In contrast, detecting a fire signal from potassium emission was not reliably possible in a practically useful way. We furthermore retrieved fire temperatures by modeling the at-sensor radiance as a linear mixture of two emitted and two reflected spectral radiance endmembers. High-temperature fire areas (the high-intensity fire front, modeled at 800-900 K) and low-temperature combustion (residual fire at 500-600 K), were mapped. High-temperature burning areas as small as half a percent of a Hyperion pixel (approx. 5 m^2) were detectable. These techniques are of potential interest for fire characterization in the boreal areas of the circumpolar North using current and future satellite-borne imaging spectrometers.

[1] Corresponding author, email: cwaigl@alaska.edu

1. Introduction

Satellite-based infrared remote sensing has been in use since the 1980s as a cost-effective way to detect and investigate wildfires (e.g. Flannigan and Haar, 1986; Robinson, 1991; Prakash et al., 2011; Ichoku et al., 2012). Multispectral sensors, which typically offer a small number of carefully placed spectral bands, are widely used. For the detection of radiation emitted by active fire, the mid- and thermal infrared (MIR and TIR) regions of the electromagnetic spectrum are of particular interest (Kaufman et al., 1998; Briess et al., 2003; Giglio et al., 2003, 2016; Schroeder et al., 2014) as the fire-emitted radiance in the MIR range (approximately 4 μm) far exceeds background levels even if fire only occupies a small portion of a pixel. Other techniques employ shortwave infrared (SWIR) data from sensors with a spatial resolution of approximately 30 m and suitable sensitivity and saturation behavior (Giglio et al., 2008; Schroeder et al., 2015).

In contrast, in imaging spectroscopy (also called hyperspectral remote sensing), data is acquired in a large number of contiguous spectral bands that typically span the visible and near-infrared (VNIR) as well as the shortwave infrared regions of the electromagnetic spectrum. Given that an imaging spectrometer produces a radiance or reflectance spectrum at every pixel of the image, a frequently used approach consists in unmixing these spectra using spectral libraries of relevant land cover classes (Roberts et al., 1998). Imaging spectroscopy has been applied to wildfire analysis with respect to pre- and post-fire research topics such as vegetation classification (Goodenough et al., 2003; Dennison et al., 2006; Dalponte et al., 2013), fire danger (Roberts et al., 2003), forest canopy fuel characteristics (Jia et al., 2006) and fire severity (Lewis et al., 2011). Nearly all of these works use airborne hyperspectral imagery. Studies of high-temperature events that are relevant to satellite-based hyperspectral remote sensing include applications to volcanology (Wright et al., 2010; Abrams et al., 2013), fire detection (Dennison, 2006; Dennison and Roberts, 2009; Amici et al., 2011) and fire characterization via fire temperature and fractional pixel area retrieval (Dennison et al., 2006; Dennison and Matheson, 2011). These studies rely on the spectral emission and absorption features, sensitivity, and large number of data points produced by the hyperspectral instrument instead of MIR or TIR bands, which are generally not available.

Active fire in the boreal forest is currently not well-studied using imaging spectroscopy despite the fact that wildland fire is an important factor in the boreal forest eco-region (Chapin et al., 2000). For Alaska, where a majority of the boreal areas of the United States of America is located, wildfires consume an average of 7500 km^2 annually (Kasischke et al., 2010). The average annual burned area has been estimated to increase by 2.4 %/yr (Calef et al., 2015, for 1943-2012) to 3.1 %/yr (Giglio et al., 2013, for all of boreal North America, 1995-2011).

The Hyperion sensor on the National Aeronautic and Space Administration's (NASA's) EO-1 (Earth Observation 1) satellite platform (Pearlman et al., 2003; Ungar et al., 2003; Middleton et al., 2013) offers an opportunity to fill this gap and develop methodologies that will be more useful as future imaging spectrometers become available. Currently, planned missions are NASA's Hyperspectral Infrared Imager (HyspIRI) (Middleton et al., 2010; Abrams et al., 2013; Lee et al., 2015), the German Environmental Mapping and Analysis (EnMAP) instrument (Kaufmann et al., 2006), the Italian Space Agency's (ASI's) PRecursore IperSpettrale della Missione Applicativa (PRISMA) satellite (Labate et al., 2009), and the Spaceborne Hyperspectral Applicative Land and Ocean Mission (SHALOM) (Ben Dor et al., 2014; Feingersh and Ben Dor, 2015), a collaboration of the space agencies of Israel and Italy. All of these missions will offer a spatial resolution comparable to Hyperion, a similar range of spectral channels, and reduced noise. The main objectives of both PRISMA and SHALOM include gathering information about land cover, pollution and the carbon cycle. EnMAP is equipped with pointing capability of $\pm$ 30° to achieve a target revisit frequency of 3-4 days and aims to measure parameters related to biochemical processes (Kaufmann et al., 2006). Wildfire is a factor in all these topics. HyspIRI will also include a multispectral TIR instrument to enhance the instrument's ability to investigate high-temperature targets (Roberts et al., 2012; Realmuto et al., 2015). Its revisit frequency is 16 days for VNIR/SWIR and 5 days for TIR globally, but less at high latitudes. HyspIRI was designed to address science questions about wildfire in relation to vegetation cover as well as global biomass burning (Realmuto et al., 2015).

The operational community does not currently use hyperspectral data for fire detection. While TIR sensors are traditionally the instrument of choice for fire detection especially on a global scale, we find that the detection of low-intensity active fire is often not satisfactory in existing fire products (Waigl et al., 2017). The new hyperspectral sensors in development will be capable of covering larger regions of the earth with exceptional spatial, spectral, and temporal resolutions. They will provide greatly enhanced signal-to-noise ratio and target revisit capabilities. The main objective of this study is to evaluate existing fire detection methods and the capabilities imaging spectroscopy. Our research aims to identify spectral bands that can be proposed for future hyperspectral and multispectral instruments.

We explore the application of satellite-based imaging spectroscopy to the study of the properties of active fires in Alaska's boreal forest. In the following sections, we introduce our three study areas, which are located in interior Alaska, and provide an overview of the available Hyperion data. We then describe three known fire detection methods that have the potential to be applicable to our study scenes: the Hyperspectral Fire Detection Index (HFDI), the detection of a potassium (K) emission feature, and the carbon dioxide continuum-interpolated band ratio (CIBR), which relies on the measurement of an absorption feature to differentiate between emitted and reflected radiation. We also describe how sub-pixel active fire temperatures and fractional areas are retrieved using a linear combination of simulated atmospherically corrected emission spectra and reflected background spectra. The description of methods is followed by a summary of results and their discussion. We conclude by evaluating our findings with a view on how these methods could be applicable to future satellite-borne hyperspectral sensors and which design features might be particularly beneficial for active boreal forest fire remote sensing.

2. Study Areas

We selected three study areas (Figure 1) based on the availability of EO-1 Hyperion data over large Alaskan wildfires. We searched the catalog of available scenes in the United States Geological Survey (USGS) data archive based on fire location and time data from the Alaska Large Fires Database (ALFD) (Kasischke et al., 2002) and subsequently selected all scenes that clearly showed several clusters of contiguous pixels with active combustion that were not obscured by smoke or clouds. The selected scenes represent the 2004 Boundary fire, the 2004 Crazy fire, and the 2009 Wood River fire.

With a burned area of 2150 km^2, the 2004 Boundary fire north of Fairbanks, Alaska, was the largest wildfire of the most extreme Alaska fire season on record: During the summer of 2004, a total of 27 000 km^2 burned in approximately 700 separate fire events (AICC, 2004). The Boundary fire, discovered on June 13, 2004, was a highly destructive lightning-caused event which greatly impacted air quality (Grell et al., 2011) and aerial traffic across interior Alaska (Wendler et al., 2010), and was sufficiently severe to affect the post-fire succession of tree species in the boreal forest (Johnstone et al., 2010).

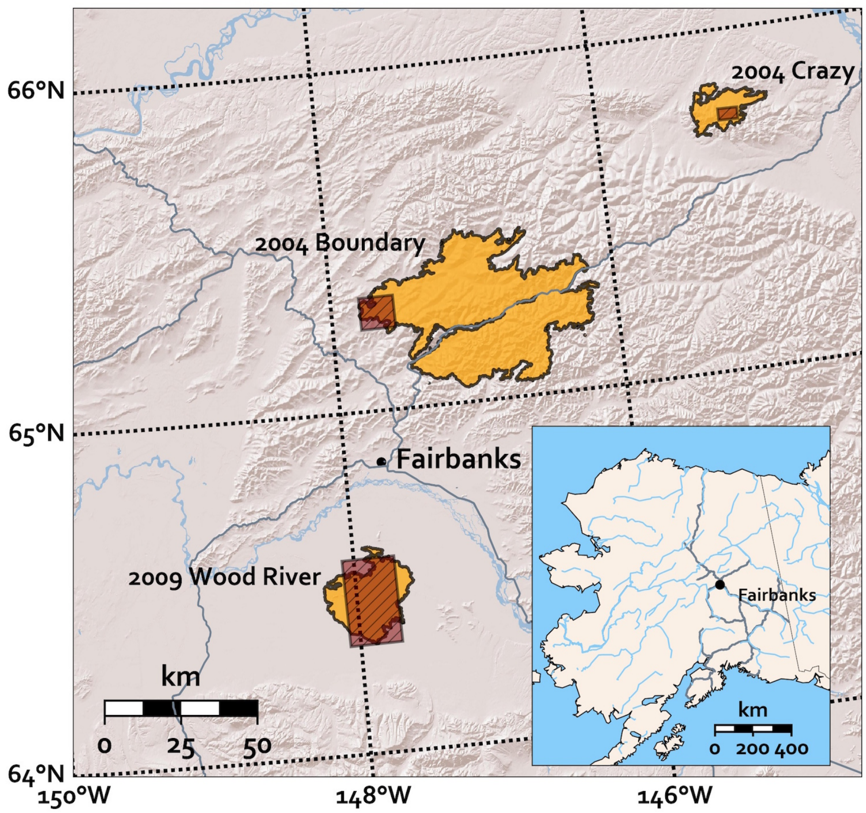

Figure 1: Map of study areas and corresponding final fire perimeters within interior Alaska. The rectangular areas represent the three Hyperion study scenes. Fire perimeters are from the Alaska Large Fires Database (ALFD), maintained by the Alaska Interagency Coordination Center, and typically digitized from Landsat data (30 m resolution). Rivers and major roads are marked.

The 2004 Crazy fire was a smaller fire event (final burned area: 210 km^2) whose active period overlapped with the Boundary fire. It started from a lightning-caused ignition on July 4, 2004, approximately 75 km north-east of the Boundary fire.

The Wood River fire of 2009 also had air quality impact on Fairbanks. It burned in an area reserved for military use south of the town. Its final size is given as approximately 500 km^2 (AICC, 2009), but its burn perimeter includes considerable unburned areas. (The official designation of this fire event is ”Wood River 1”, but we omit the number for the sake of readability.)

The land cover in all three study areas is dominated by highly flammable black spruce forest. Stand density is much lower for the Wood River fire, which burned through a mix of forest and open brush land. The landscape is wetter and flatter than for the Boundary or the Crazy fire, located in hilly areas at higher elevations (500 to 1000 m above mean sea level). The Boundary fire also affected mixed conifer and hardwood stands.

3. Data

3.1. The Hyperion sensor on EO-1

The Hyperion sensor is a pushbroom instrument with a 7.7 km wide imaging swath and a ground-sampling distance (GSD) of 30 m (Ungar et al., 2003). It is composed of two separate spectrometers: A VNIR instrument (400 - 1000 nm) and a SWIR instrument (1000 - 2500 nm), both with a spectral bandwidth of 10 nm (Figure 2) (Barry, 2001). In total, it has 242 spectral bands, with VNIR and SWIR channels overlapping around 1000 nm. Due to the moderate signal-to-noise ratio (SNR), which deteriorates in the SWIR region compared to the VNIR, only 198 unique calibrated usable channels – 50 VNIR and 148 SWIR – are processed in the Level 1B product (Pearlman et al., 2003). The longest-wavelength calibrated channel is band 224 (central wavelength 2395.5 nm). All throughout the extended mission phase, the Hyperion mission has continued to support calibration and validation activities such as improved lunar and terrestrial vicarious calibration technology and noise characterization (Kerola et al., 2009; Middleton et al., 2010).

Originally conceived as a 1-year technology demonstration, the EO-1 mission went through several extensions (Middleton et al., 2013) after its initial operational phase (11/2000 – 2/2002) was completed. Orbital parameters were not preserved throughout the extensions. The data for the 2004 Boundary and Crazy fires were acquired during the initial extended phase that ended in late 2005, during which the EO-1 spacecraft was maintained in a 705 km orbit. In 2006, EO-1 was lowered until it reached an orbital height of 690 km, at which point, in 2007, the mission was revived (Middleton et al., 2013). The 2009 Wood River study scene was acquired during the phase that followed. 2016 was EO-1's last operational year.

Hyperion data is distributed as 12-bit unsigned integer raster data, which is radiometrically and terrain-corrected (Simon, 2006).

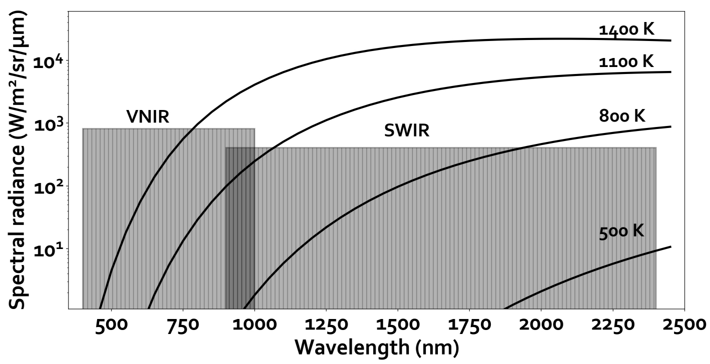

Figure 2: Wavelength range of the VNIR and SWIR instruments of the Hyperion sensor. Some blackbody spectra are superimposed for comparison.

3.2. Hyperion scenes

For all three study scenes, the Hyperion scene reference, scene start time stamp, sensor look angle and latitude/longitude of the center of the used subset are summarized in Table 1. All overpasses took place within 20 min of 1 pm Alaska Daylight Time, on a descending node.

The Hyperion scene available for the Boundary fire was acquired on July 19, 2004 and captures a small portion of the fire close to the western boundary of the final fire perimeter (Figure 1). Between the peak of the fire event on July 17 and the overpass of the EO-1 satellite two days later, traces of precipitation halted its progress. The Hyperion imagery for the Crazy fire was acquired on July 10, 2004, when it was highly active.

The third study scene was acquired over the Wood River fire on August 2, 2009, during a high-intensity phase of the fire event. Unfortunately, the Hyperion swath missed the most active portions of the fire front and only captured a number of relatively small fire pixel clusters, which are also spread over a larger area than in the 2004 Crazy and Boundary fire scenes. The 2009 data also appears to contain more noise and more pronounced pushbroom stripes than the earlier scenes. Therefore, we do not present any detailed maps of fire detection or temperature retrieval over this scene. However, the Wood River data was included in the evaluation of fire detection indices.

Table 1: EO-1 Hyperion scenes and central latitude/longitude (WGS 84) of the subsets used

Fire name	Fire start date	Hyperion scene	Scene start time (UTC)	Sensor look angle	Latitude	Longitude
Crazy	2004-07-04	EO1H0680132004192	2004-07-10 21:07:57	10.358°	65.74979°	-145.0569°
Boundary	2004-06-13	EO1H0690142004201	2004-07-19 21:02:11	-2.4442°	65.28703°	-147.7966°
Wood River	2009-07-12	EO1H0690142009214	2009-08-02 20:40:37	-16.446°	64.44595°	-147.8978°

4. Methods

Our Hyperion processing steps are summarized in Figure 3. After subsetting the swaths to the study areas, the digital numbers were converted to spectral radiance by dividing them by the scaling factors of 40 for the VNIR bands and 80 for the SWIR bands, specified in the scene metadata (Simon, 2006). The theoretical upper limits for measurable radiance are 819.2 $\mathrm{W/(m^2\,\mu m\,sr)}$ (VNIR) and 409.6 $\mathrm{W/(m^2\,\mu m\,sr)}$ (SWIR), respectively.

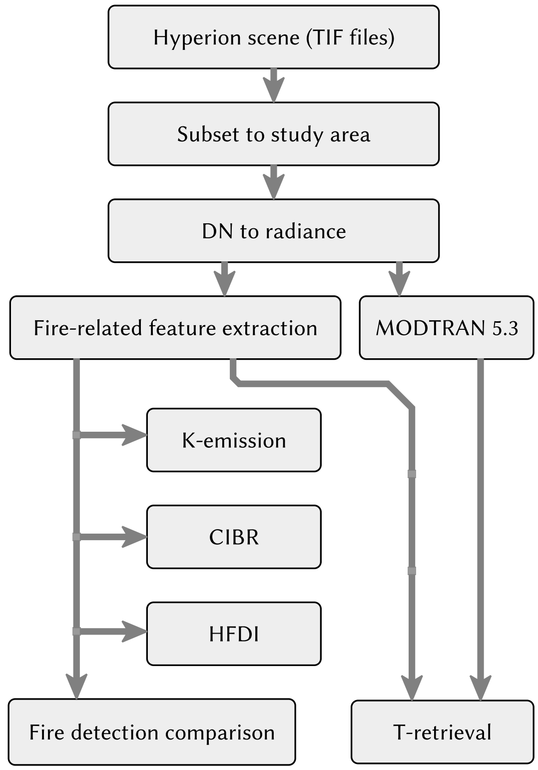

Figure 3: Hyperion processing flow

4.1. Fire-related feature extraction

The evaluation and comparison of fire detection methods requires labeled fire and non-fire pixel data, which we generated by applying supervised classification to the study scenes. We used a false natural-color RGB image of each scene (bands 150-50-23, with central wavelengths of 1648.9 nm, 854.18 nm, and 579.45 nm) to manually sample 20 pixels from each of the following four classes: fire, fresh fire scar, vegetation (forest or forest/shrubland), smoke/cloud. We carefully selected areas that were as pure as possible, avoiding mixed land cover classes and data anomalies such as saturation effects. By "fire" we mean pixels that contain actively burning areas. The Crazy fire imagery contained enough of both smoke and cloud that 20 pixels from each class were sampled, whereas the Wood River imagery is virtually smoke/cloud free, so the class was not sampled.

We further constrained the study areas more narrowly to the fire-adjacent region with the help of a mask: We first applied a spectral radiance threshold of 5 $W/(m^2\ \mu m\ sr)$ in band 220 (2355.21 nm) based on the observation that the spectral radiance of known non-fire pixels remains below this value. For the Crazy fire scene, we also excluded cloud pixels, which are highly reflective in the SWIR. Then we drew a convex shape around the set of all pixels exceeding the threshold, with an added 20 pixel wide buffer. The resulting mask ensures that only data located in the vicinity of active fire was processed. The pixels contained in these irregularly shaped subsets were classified with a Random Forest classifier (Breiman, 2001), a supervised classification method that has been successfully applied to Hyperion data (e.g. Ham et al., 2005). The manually labeled sample pixels served as training data. To assess the stability of the classifier and confirm the adequacy of using 20 training samples per class, we carried out a K-fold cross-validation (K = 10) (Friedman et al., 2001).

The pixels in the "fire" class served as a data source for labeled fire pixels to evaluate fire detection methods, while the "vegetation" and "fire scar" classes represented the non-fire background. The "fire" class also was used as the input for fire temperature retrieval.

4.2. Fire detection

Fire detection in imaging spectroscopy data can use a number of different approaches. One is to rely on the same methods as fire detection in multi-spectral imagery: to identify thermal anomalies based on the electromagnetic radiation emitted by a burning source. If we represent the fire as a blackbody held at a constant temperature, the emitted spectral radiance is given by Planck's law:

$$L_\lambda = \frac{2hc^2}{\lambda^5 \left(e^{\frac{hc}{\lambda kT}} - 1\right)} \quad (1)$$

with T the absolute temperature, λ the wavelength, $h = 6.626\,070\,04 \times 10^{-34}\ \mathrm{m^2kg/s}$ Planck's constant, $k = 1.380\,648\,52 \times 10^{-23}\ \mathrm{m^2kg/(s^2K)}$ Boltzmann's constant and $c = 2.997\,924\,58 \times 10^{8}\ \mathrm{m/s}$ the speed of light. With increasing temperature, the maximum of the emission curve moves towards shorter wavelengths, in a relation that is inversely proportional to the temperature (Wien's law):

$$\lambda_{\max} = \frac{b}{T}, \quad (2)$$

in which $b = 2897.7729$ μmK is Wien's displacement constant.

Compared to a fire-free pixel, the overall spectral radiance in the longer SWIR wavelengths is therefore elevated whenever a pixel contains fire activity.

Alternatively, hyperspectral remote sensing can make use of features that are caused by potassium emission and carbon dioxide absorption (Vodacek et al., 2002; Dennison and Roberts, 2009; Amici et al., 2011; Dennison, 2006).

We tested and, where necessary, adapted three known fire detection indices for hyperspectral data, each time proceeding in an identical fashion: Between all test scenes, we randomly sampled 250 fire pixels (from the "fire" class) and 250 background pixels (from the "vegetation" or "fire scar" class), calculated each index for all sample pixels and statistically analyzed the result for its ability to differentiate fire and background. We calculated all fire detection indices based on at-sensor spectral radiances that were uncorrected for atmospheric effects as a first approximation. During our analysis we also tested combinations of two or all three indices to maximize detection accuracy and minimize false detections (errors of commission).

4.2.1. *Potassium (K) emission*

This method uses the potassium (K) emission lines at 766.5 and 769.9 nm (Vodacek et al., 2002) characteristic for biomass burning. In Hyperion data, both emission lines fall within band 42 with a central wavelength of 772.78 nm. Its spectral radiance would be elevated in the presence of fire-stimulated potassium emissions (Cahill et al., 2008), but the neighboring band at 780 nm would not be.

Dennison and Roberts (2009) define a K-emission index as the ratio L_{770nm}/L_{780nm} and use it with data from the Airborne Visible / Infrared Imaging Spectrometer (AVIRIS), while Amici et al. (2011) examine high spectral resolution as well as simulated and real Hyperion data using a metric called the Advanced K-Band Difference (AKBD). In Hyperion data the AKBD metric translates to the band difference $L_{770nm} - L_{780nm}$.

Values for the K-emission ratio are expected to be <1, and AKBD values <0. This is because the 770 nm band is also the location of multiple oxygen absorption lines which overlap with the K-emission features (Vodacek et al., 2002) and, averaged over the width of the 770 nm Hyperion band, lead to a distinctly visible absorption feature (Amici et al., 2011).

4.2.2. *Carbon dioxide continuum-interpolated band ratio (CO_2 CIBR)*

The second fire detection method makes use of the CO_2 absorption feature at 2010 nm. It takes advantage of the principle that radiation emitted by a fire only has to travel through the atmosphere once to arrive at a satellite-borne sensor, whereas reflected sunlight traverses the atmosphere twice. Emitted radiation at this spectral location therefore undergoes less absorption than reflected radiation. Therefore, for fire pixels, the CO_2 absorption line should appear less pronounced than for background pixels. Mathematically, the depth of the absorption line is captured by defining an index called the carbon dioxide continuum-interpolated band ratio (CO_2 CIBR) (Dennison, 2006; Dennison and Roberts, 2009), used successfully for fire detection with Hyperion and AVIRIS data. As the absorption feature is located on an upslope section of the radiance spectrum, the two shoulders of the feature are not typically at the same value. This situation is reflected via interpolation factors used in the formula provided by Dennison (2006):

$$\mathrm{CIBR} = \frac{L_{2010\,\mathrm{nm}}}{0.666\,L_{1990\,\mathrm{nm}} + 0.334\,L_{2040\,\mathrm{nm}}} \tag{3}$$

4.2.3. Hyperspectral fire detection index (HFDI)

The third approach uses a normalized difference index calculated from the spectral radiance values in two suitable SWIR bands, which enables the detection of pixels that contain thermal anomalies. (Dennison and Roberts, 2009). Dennison and Roberts (2009) found the following HFDI performing the best on AVIRIS data for daytime detection of the Simi Fire in California:

$$\mathrm{HFDI} = \frac{L_{2430\,\mathrm{nm}} - L_{2060\,\mathrm{nm}}}{L_{2430\,\mathrm{nm}} + L_{2060\,\mathrm{nm}}} \tag{4}$$

A threshold for detection is determined at a value that optimally separates fire pixels from non-fire pixels; it is typically close to zero, or has a small negative value (Dennison and Roberts, 2009).

The original HFDI cannot be used without modification as the longer wavelength (2430 nm) exceeds the longest wavelength available in Hyperion's L1B calibrated spectral radiance product. After inspecting the spectra for saturation behavior, we identified ranges of candidate bands in the vicinity of the shorter and longer wavelengths of Eq. (4) and constructed a modified HFDI from the average of normalized difference values of band combinations that best separate fire from non-fire pixels.

4.3. MODTRAN for atmospheric correction

Active fire temperature retrieval requires atmospherically corrected sources of emitted infrared radiation. We used MODTRAN 5.3 (Berk et al., 2006) to generate transmittance profiles for each study scene across the wavelength region between 350 and 2500 nm. The MODTRAN input was based on user-specified model atmosphere from radiosonde data acquired at noon on the day of the respective overpass at Fairbanks International Airport (PAFA station) distributed by the University of Wyoming Atmospheric Sciences Department (http://weather.uwyo.edu/upperair/sounding.html). Due to the presence of active fire, and therefore smoke, in the study scene, we selected the predefined option "rural extinction, visibility 5 km". Additional MODTRAN input parameters are summarized in Table 2.

The transmittance profiles were then used to generate a set of simulated atmospherically corrected blackbody radiance spectra to serve as temperature endmembers in a linear model.

4.4. Temperature retrieval

The spectrum measured at the pixel that is the site of active fire can be modeled as a linear mixture of emitted and reflected components (Dennison et al., 2006). We represented the measured at-sensor spectral radiance $L_{\lambda,m}$ as the sum of signals that originate from a number n of fractional areas each of which burns at a constant temperature T_i, plus uniform background components:

Table 2: Configuration used with MODTRAN 5.3

Parameter	Comment
MODEL = 7	User-specified model atmosphere from radiosonde data (PAFA station, noon)
ITYPE = 2	Vertical or slant path between two altitudes
IHAZE = 2	RURAL extinction, default VIS = 5 km
IEMSCT = 0	Spectral transmittance mode only
CO2MX = 390.0	CO_2 mixing ratio
H1 / GNDALT	Determined from altitude of center of subset
H2	Determined from highest level available in radiosonde profile
ANGLE	Determined from sensor look angle
V1 = 350	Initial wavelength (nm)
V2 = 2500	Final wavelength (nm)
DV = 1	Wavelength step (nm)

$$L_{\lambda,m} = \sum_{i=1}^{n} p_{i,\text{fire}} L_\lambda(T_i) + \sum_{j=1}^{m} p_{j,\text{background}} L_{j,\text{reflected}} \tag{5}$$

$L_\lambda(T_i)$ is the atmospherically corrected spectral radiance of the temperature component T_i, $L_{j,\text{reflected}}$ is the jth background component, and the p_i and p_j are the corresponding fractional pixel areas, which have to add up to 1. Atmospheric scattering was taken into account via the IHAZE parameter in the MODTRAN transmittance calculation (Section 4.3, Table 2). Otherwise, path radiance was neglected (following e.g. Dennison and Matheson, 2011). This approach is similar to the two-component sub-pixel temperature and fractional area retrieval method developed by Dozier (1981) using mid- and thermal infrared data; the uncertainties in retrieved fire temperature and fractional area increase substantially when the fractional fire area becomes very small (Giglio and Kendall, 2001).

In order to select suitable background components $L_{j,\text{reflected}}$ we considered that the reflected contribution dominates in the VNIR spectral range. To reduce the influence of the reflected radiation components and scattering by smoke at shorter wavelengths we limited the analysis to all wavelengths λ >1400 nm (100 calibrated Hyperion channels). In the vicinity of active fires, we are likely to find two physically distinct background landcover types: vegetation and fire scar. After inspecting SWIR spectra from the "vegetation" and "fire scar" classes, we found them to be quite distinct, at least in the shorter wavelength part of the SWIR range (between 1400 and 1800 nm) and therefore opted for two separate background contributions ($m = 2$). The $p_{j,\text{background}}$ become the fractional areas p_{veg} and p_{scar}.

For the emitted components $L_\lambda(T_i)$ we used Planck blackbody spectra which we atmospherically corrected using the MODTRAN 5.3 transmittance profiles calculated for each acquisition date. For each study case, a catalog of these temperature endmembers was generated covering the temperature range between 40 K and 1200 K in steps of 10 K.

To determine the parameters T_i and p_i we used least-squares curve fitting for the set of all pixels in the "fire" class. The best-fitting n temperature endmembers are retained as modeled temperature components. Regarding the choice of n, Dennison et al. (2006) used a single temperature component, but at a much higher spatial resolution (AVIRIS GSD of 5 m instead of 30 m for Hyperion) which is more likely to be adequately described by a single fire temperature. A different example comes from an application to lava temperatures using Hyperion data (Wright et al., 2010; Abrams et al., 2013), where an n of 2 or 3 yielded a satisfactory fit. We started with a single temperature component followed by an increase of n to 2, checking whether the RMS error improved.

In our model, $m = 2$ and $n = 2$ means fitting five parameters to 100 Hyperion SWIR data points (T_1, $p_{1,\text{fire}}$, T_2, $p_{2,\text{fire}}$ and p_{veg}, with p_{scar} determined via the constraint that the sum of all fractional areas must be 1). Even though it would appear that there is no risk of overfitting, there are strong arguments against further increasing n: The spectral radiance values of a Hyperion SWIR spectrum are not arbitrary, but correlated with each other. They are also affected by sensor noise, and we made a number of simplifying assumptions (that the fire targets are blackbody radiators, that path radiance is minimal and can be neglected, that the composition of the background is uniform). For the area footprint (900 m^2) of a Hyperion pixel, model output with two temperature components would appear to reasonably describe a physical reality, but this becomes less true when the number of temperature endmembers increases.

5. Results

5.1. Fire detection and comparative analysis

Fire, fire scar, vegetation and smoke/cloud areas (Figure 4) were delineated for each study area using a Random Forest classifier. We set the number of decision tree estimators in the classifier to 100 and verified the stability of the classification by repeat runs, observing that pixel counts in all classes remained roughly equal. Furthermore, a 10-fold cross-validation, each time with a different 60/40 split of the labeled input data into training and test sets, yielded both accuracy and F1 (macro) scores (that is the harmonic average of true positive rate and positive predictive value) of 0.97 ± 0.11. This is a good result and confirms that selecting 20 labeled training samples in each class was sufficient. The final classifications have 1019 pixels in the "fire" class for the Crazy fire test site, 662 for the Boundary fire scene, and 197 for the Wood River scene. Across the classified scenes, we randomly sampled 500 pixels for use as a labeled test set to evaluate fire detection indices (200 each from the Crazy and Boundary fire scenes and 100 from the Wood River scene, given the smaller number of fire pixels in this scene). Half the samples were drawn

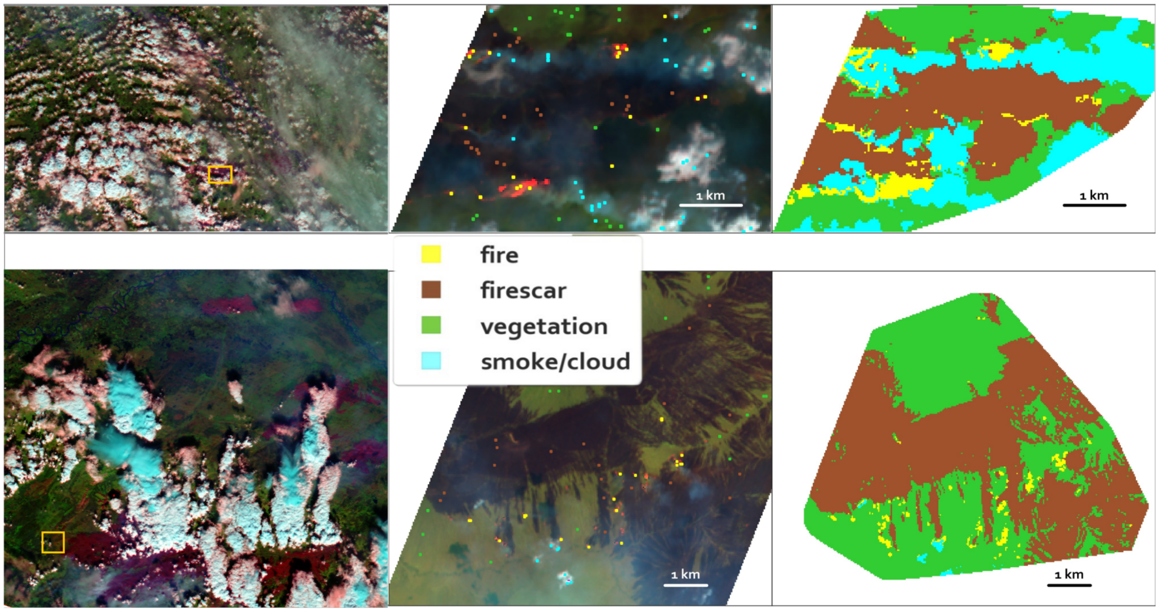

Figure 4: Crazy fire (top) and Boundary fire (bottom). Left: Overview plot from the Moderate-resolution Imaging Spectroradiometer (MODIS) on the Terra satellite, acquired the same day as the Hyperion scene. RGB composite using bands 7-2-1. The extents of the Hyperion scenes are marked by yellow rectangles (same locations as in Fig. 1). Middle: Hyperion RGB composite using bands 150-50-23 in RGB (1648.9 nm, 854.18 nm, and 579.45 nm), with manual samples marked. (Pixel color designations: yellow - fire, brown - firescar, green - vegetation, turquoise - smoke or cloud.) Right: classification output (same colors as in the middle). The irregular shape of the classified subsets (right) reflects the final subset masks, which delineate the fire-adjacent zones using a simple SWIR radiance threshold.

from the “fire” class and half from “fire scar” or “vegetation”, which together represent the “background” class for the purpose of fire detection.

Spectra from the “fire” class that are free from anomalies or saturation effects can be distinguished from background pixels by observing the spectral radiance values in the SWIR range: Unlike in pure background pixels, whose spectrum would continue to fall off, a contribution from emitted SWIR radiation is apparent (Figure 5 a). At higher fire intensities the longer-wavelength SWIR part of the spectra saturates, reaching spectral radiances close to the theoretical maximum of 409.6 $\mathrm{W/(m^2\ \mu m\ sr)}$ (Figure 5 b) However, we observe that not all saturation effects manifest as a range of radiance values pinned

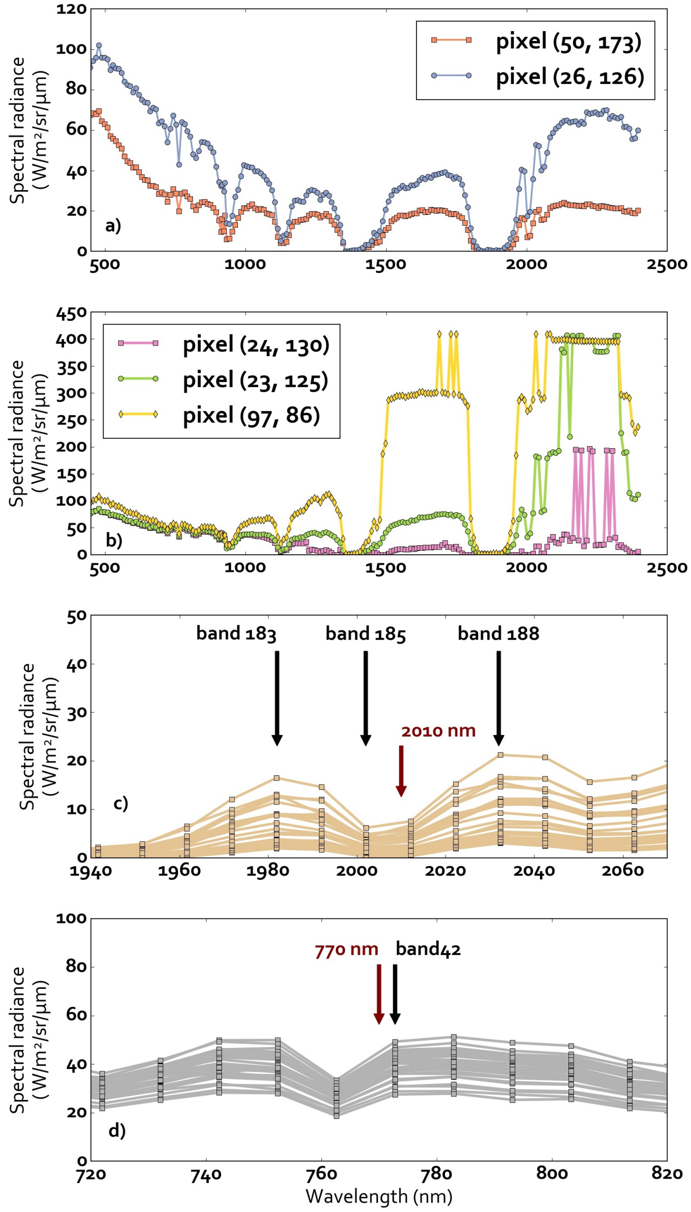

Figure 5: Examples of fire pixel radiance spectra. a) and b) represent a selection of fire pixel spectra (taken from the Crazy fire study area at the indicated pixel locations). c) and d) show the theoretical absorption or emission feature location and relevant bands used for fire detection with the the CO_2 *CIBR and K-emission methods, respectively.*

to the theoretical maximum: in some pixels, and even at radiance levels below those of the most intense fires, individual bands exhibit spikes (which may or may not extend all the way to the saturation maximum) even when neighboring bands do not. This may be due to potential differences in the lag time between saturation and becoming operational again for individual Hyperion detector elements.

The CO_2 absorption feature used for calculating the CO_2 CIBR index is markedly present at approximately the expected location (Figure 5 c). After data inspection, we used bands 183 at 1981.86 nm and 188 at 2032.35 nm for the shoulders of the absorption line, and band 185 at 2002.06 nm, where the minimum of the absorption feature was consistently located, for its center. In contrast, no K-emission feature in band 42 is discernible with the naked eye (Figure 5 d).

We then evaluated all three indices over the labeled test set of 500 sample pixels (Figure 6). For the HFDI, band 224, with a central wavelength of 2395.5 nm, is the longest-wavelength calibrated band, and we found the top of the Hyperion band range, beyond approximately band 220, to be extremely noisy. As for the shorter wavelength used to construct the published HFDI (Dennison and Roberts, 2009), 2060 nm is closest to Hyperion's band 191. To consider a range of candidate bands for a Hyperion-based HFDI we selected all combinations of shorter-wavelength and longer-wavelength bands that can be generated from any of the bands 190, 191, 192, 193, 194, 195, and 196 as the shorter-wavelength band and any of the bands 217, 218 and 219 as the longer-wavelength band. We thereby avoided the bands in the middle of the spectral radiance "plateau", which are often affected by anomalies and saturation effects (Figure 5).

It was apparent that for an HFDI calculated with band 190 as the shorter-wavelength band, both the variance of HFDI values and the separation of fire and background HFDI values was worst, likely due to sensor noise in band 190. To further quantify the available choices for a Hyperion-specific HFDI, we modeled the distribution of HFDI values in both the fire and background class for each combination as normal distributions and calculated their overlap (which represents the sum of all errors of commission and of omission), the

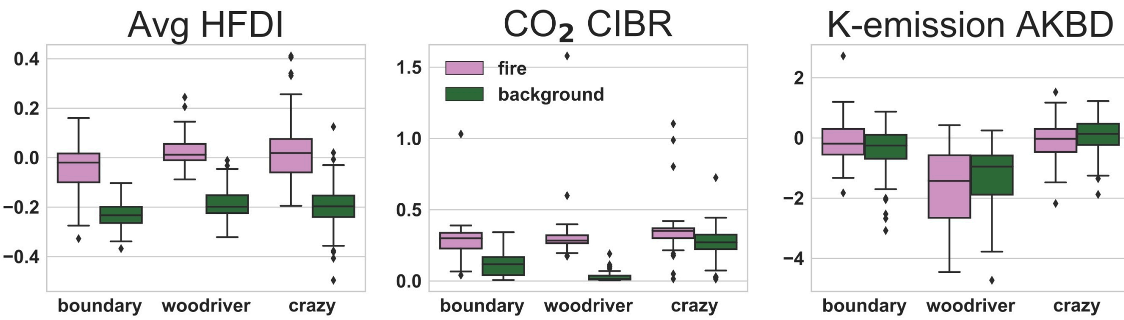

Figure 6: Comparison (box plots) of the distributions of average HFDI, carbon dioxide CIBR and K-emission band difference index across fire and background pixels for each fire event. The whiskers extend to the highest and lowest datum still within 1.5 times the inter-quartile range. Data points beyond this range are plotted as outliers.

optimal cut-off value to separate fire from background, as well as the positive predictive value and the F1 score (Table 3), which takes into account both errors of commission and of omission.

Several potentially "best" combinations obtain very similar results in positive predictive value and F1 score and there is no clear cut-off other than removing band 190 from consideration. We therefore discarded the three combinations of band 190 with bands 217 to 219 and averaged the remaining 18 HFDI combinations. Averaging the indices calculated from multiple bands has the advantage of reducing the influence on single-band noise on the resulting mean index value. For this "average HFDI" (Figure 6), we found an optimal cut-off value to separate fire from background of -0.13, based on our data.

The CO_2 CIBR index is also capable of separating fire from background (Figure 6), albeit with notable differences between the three study areas (Figures 6 and 7). This index also produces some extreme outliers. Between all 500 samples, the optimal CO_2 CIBR value to separate fire from background was determined to be 0.21. As for the K-emission index, we found no statistical ability to distinguish fire from background (Figure 6). For two of the test scenes, the median index value is even (slightly) greater for the background pixels than for the fire pixels.

Table 3: HFDI band combinations evaluated for 500 labeled sample pixels (fire and background). The cut-off column refers to the optimal HFDI value to separate fire from non-fire. The overlap column represents the modeled overlap between the fire and non-fire distribution. The true detection rate is the true positive rate calculated for fire detection. PPV represents the positive predictive value for fire detection.

Bands	Central λ (nm)	Cut-off	Overlap	True detection rate	PPV	F1 score
196, 217	2113.04, 2324.91	-0.172	0.138	0.868	0.879	0.873
196, 218	2113.04, 2335.01	-0.192	0.146	0.864	0.882	0.873
195, 218	2102.94, 2335.01	-0.192	0.143	0.86	0.885	0.872
195, 217	2102.94, 2324.91	-0.152	0.149	0.84	0.901	0.87
196, 216	2113.04, 2314.81	-0.172	0.134	0.84	0.897	0.868
195, 216	2102.94, 2314.81	-0.172	0.144	0.836	0.889	0.862
194, 218	2092.84, 2335.01	-0.172	0.169	0.836	0.878	0.857
193, 218	2082.75, 2335.01	-0.152	0.177	0.84	0.868	0.854
193, 217	2082.75, 2324.91	-0.111	0.185	0.812	0.894	0.851
194, 217	2092.84, 2324.91	-0.131	0.161	0.816	0.887	0.85
194, 216	2092.84, 2314.81	-0.152	0.149	0.824	0.873	0.848
192, 216	2072.65, 2314.81	-0.051	0.175	0.812	0.886	0.848
193, 216	2082.75, 2314.81	-0.131	0.172	0.828	0.855	0.841
192, 218	2072.65, 2335.01	-0.071	0.18	0.82	0.861	0.84
192, 217	2072.65, 2324.91	-0.051	0.184	0.828	0.848	0.838
191, 218	2062.55, 2335.01	0.03	0.215	0.82	0.82	0.82
191, 216	2062.55, 2314.81	0.051	0.21	0.804	0.824	0.814
191, 217	2062.55, 2324.91	0.071	0.222	0.792	0.822	0.807
190, 218	2052.45, 2335.01	0.071	0.313	0.792	0.692	0.739
190, 216	2052.45, 2314.81	0.111	0.318	0.728	0.728	0.728
190, 217	2052.45, 2324.91	0.111	0.334	0.764	0.687	0.723

We tested whether fire detection could be improved by retaining all 18 HFDI combinations separately and adding the CO_2 CIBR as well, effectively calculating a data vector of length 19 for each pixel. To evaluate the potential improvement over the averaged HFDI, we constructed a new Random Forest classifier using the 500 labeled test pixels. After executing a 10-fold cross-validation (60/40 split of the labeled samples in training and test sets) we determined a classification accuracy of 0.85 (std: 0.02) for the mean HFDI and 0.87 (std: 0.02) for the combined multi-HFDI-plus-CIBR classifier.

5.2. Temperature retrieval

The need for two separate background components was confirmed as we found that SWIR spectra from the "fire scar" and "vegetation" classes were quite distinct (Figure 8a). The distinction between the two classes was most pronounced in the shorter-wavelength SWIR region between 1400 and 1800 nm, while they vary much less in the longer-wavelength SWIR region above 1900 nm. For each study case, we used the sample-averages of the "fire scar" and "vegetation" spectra as reflective endmembers.

With a single emitted component (corresponding to three independently fitted parameters p, T, and p_{veg}), we found that the fit of fire spectra was often unsatisfactory. We therefore added a second temperature component (five independently fitted parameters, p_1, T_1, p_2, T_2, and p_{veg}), which greatly improved the result. There was no justification for adding a third temperature component.

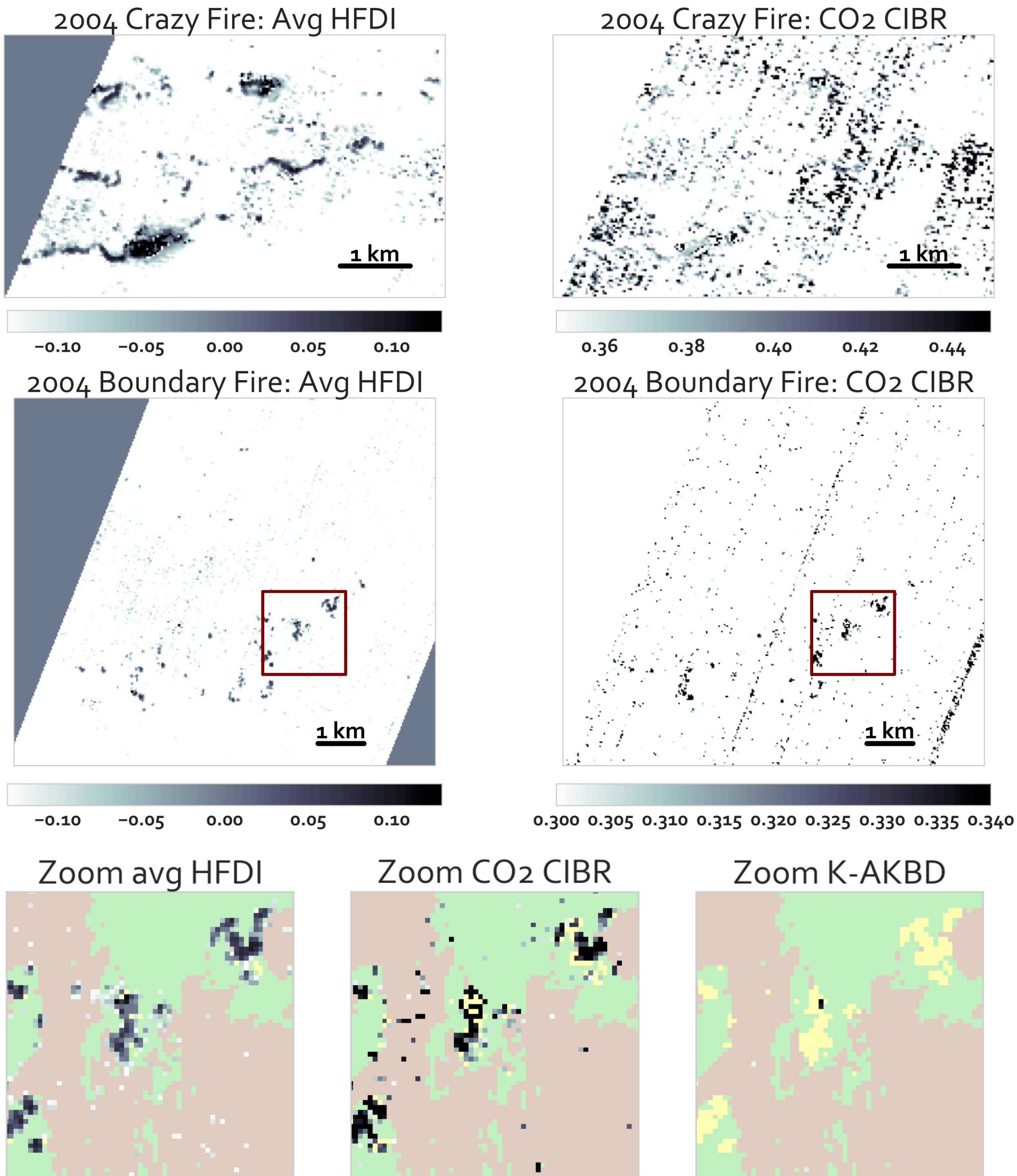

Figure 7: Values of average HFDI and CO_2 *CIBR for the Crazy and Boundary fire study areas. The stripes stem from uncorrelated striping noise typical for pushbroom sensors (Rogass et al., 2014). For the Boundary fire, the sub-region, marked by a rectangle, is enlarged (bottom row). For the enlarged region, we added the K-emission (AKBD) metric (extreme outlying values only). The colors correspond to the supervised classification, identical to Figure 4: fire (yellow), fire scar (brown) and vegetation (green). The gray (including white) values are the fire detection metrics on the same color ramp as the zoomed-out plots.*

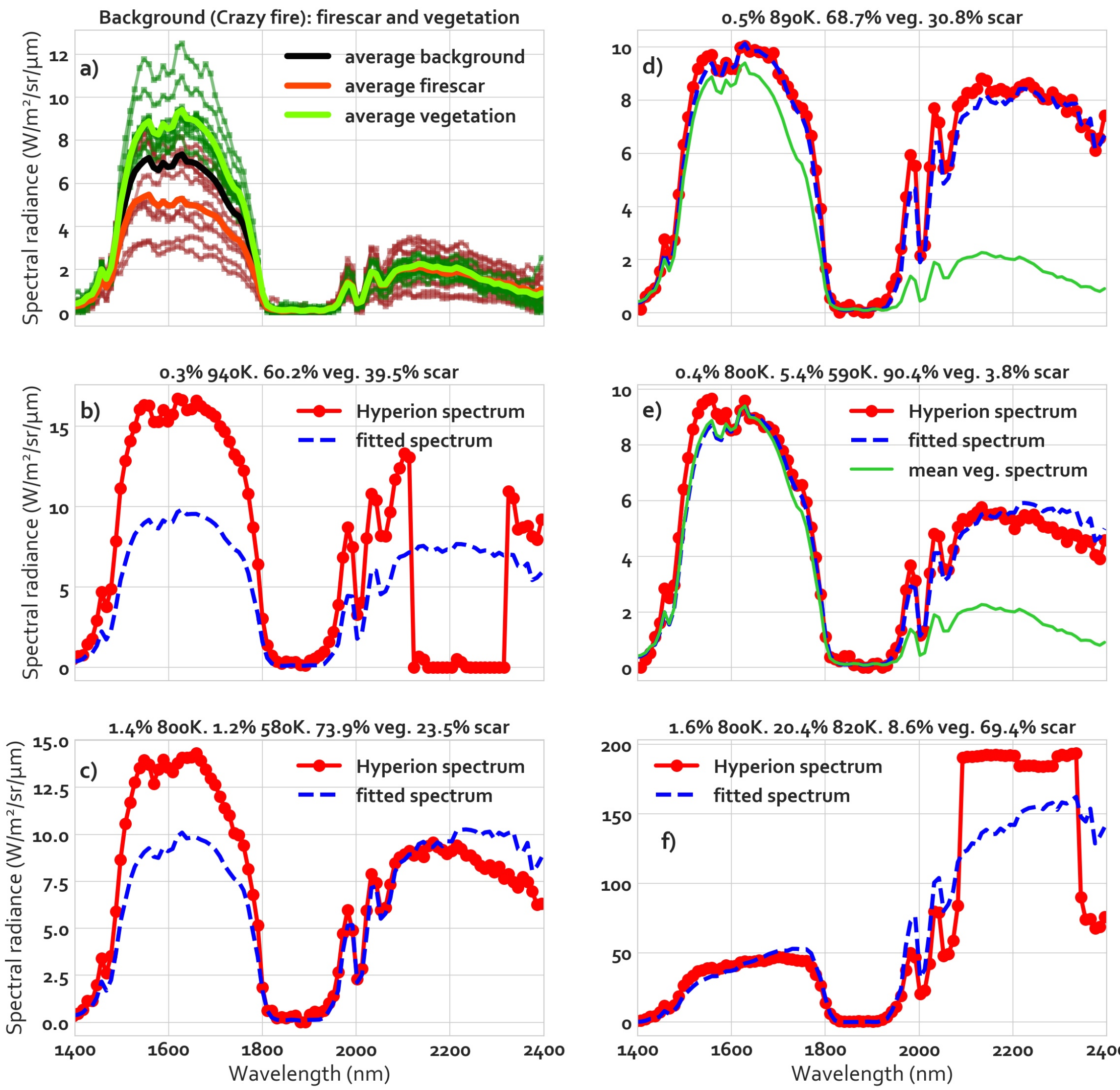

Figure 8: Example spectra for T-retrieval. a) sample spectra from vegetation and fire scar classes (green and brown), and average spectra (green, red-orange, black). b) to f) Examples of temperature and fractional area fit to individual Hyperion radiance spectra. b) and c) illustrate unsatisfactory fit in pixels with large reflective radiance contribution in the lower SWIR region, or due to data anomalies. d) to f) illustrate very good fit. In d) and e), even small fractional active fire areas are clearly distinct from pure vegetation spectra (green curve).

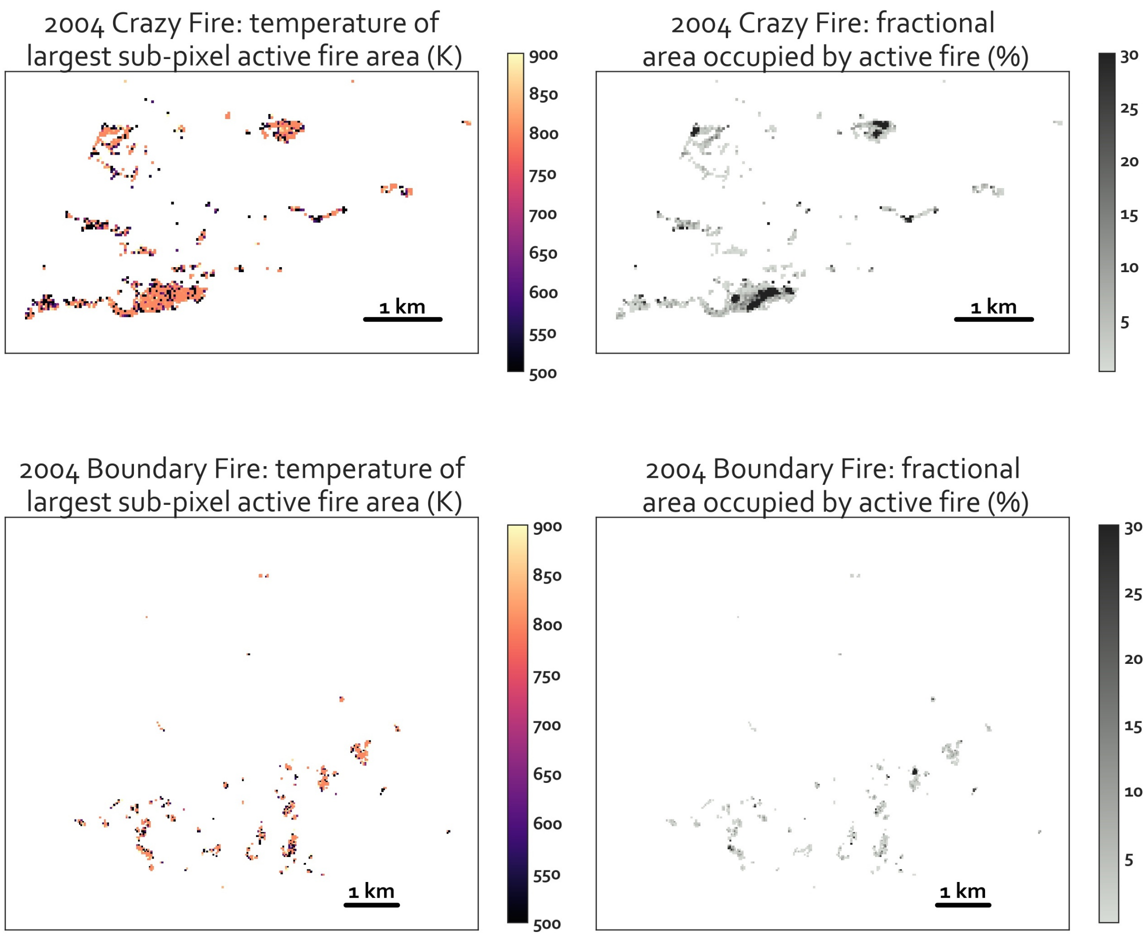

Figure 9: Burning areas of the Crazy and Boundary study sites: Temperature of the largest active fire fraction T_1 (left) and total fractional fire area $p_1 + p_2$ (right). The fire temperature map shows the most intense flaming combustion in bright colors and the pixels in which the largest fire contribution is from smoldering or other low-intensity fire in darker colors. The most intense fire front is represented by high fire temperatures on the left and high fractional areas (dark pixels) on the right. In contrast, low fire temperatures (dark tones) on the left combined with large fractional areas (dark tones) on the right would correspond a pixel that is for a large part affected by low-intensity combustion.

Typically, the fit to the measured spectra was excellent, such as in cases of pixels that are dominated by a mix of vegetation and fire scar plus either a very small fraction of relatively high-temperature fire (Figure 8d) or a slightly larger fraction of low-temperature fire (Figure 8e). Both these cases yield spectra that are essentially identical to pure background spectra in the shorter-wavelength part of the SWIR range, but deviate strongly in the longer-wavelength part. Some pixels with saturation effects are also reasonably well fitted (Figure 8f). In contrast, Figures 8b) and c) illustrate cases of relatively poor curve fit.

The retrieved temperature T_1 that corresponds to the larger active fire fraction and the total fractional fire area $(p_1 + p_2)$ are plotted in Figure 9 for the Crazy and Boundary fire scenes. (We labeled the indices so that $p_1 > p_2$.)

6. Discussion

The performance of the three fire detection methods varies. Using K-emission, we were unable to tell fire and background pixels apart. Amici et al. (2011), on the other hand, approach the method from a different angle and only look at pixels for which AKBD values are exceptionally high, which indeed, in one of the two sample scenes they examine (the 2007 Witch fire in California), enables them to detect a fire signal using Hyperion data. Following their approach, we also found an area within the the 2004 Boundary fire scene for which outliers in the AKBD metric correspond to locations of intense combustion (Figure 7, bottom row). However, the same does not apply to the 2004 Crazy or the 2009 Wood River fire, even though the Crazy fire scene contains the most intense fire across our three study sites.

Thus, even though we were able to reproduce the detection of a weak K-emission signal in one of three study cases, we cannot consider the K-emission method useful for fire detection in the Alaska boreal forest. It should be pointed out that the 2007 Witch fire was a very high intensity event that burned in chaparral shrubland near Escondido, California. This eco-region has a fire regime very different from that of a boreal forest fire in a black spruce dominated ecosystem. In the Alaska case, a large percentage of the biomass consumption comes from the sub-surface layers of organic matter (Randerson et al., 2006) rather than from quick-burning surface fuels. Furthermore, the absence of a K-emission signal even in the highest-intensity fire pixels of the Crazy fire may be related to the presence of large amounts of smoke in the scene. The active fire pixels of the 2009 Wood River fire were generally of low intensity, and a signal was not expected in this case. The main factors limiting the usefulness of K-emission with Hyperion are the much coarser spatial resolution of the satellite-borne sensor, which leads to a lowered sensitivity, and the strong sensor noise.

The carbon dioxide CIBR, which is based on an absorption feature, shows a clear statistical difference between fire and background pixels. Fire areas are discernible in a map of CO_2 CIBR values (Figure 7), but on a background of substantial noise. The Crazy fire test scene is particularly hard to map using the CO_2 CIBR, and the plot suggests that areas containing smoke or clouds, and to a lesser degree burn scars, introduce a large number of false detections. The optimal CO_2 CIBR threshold to distinguish fire from background appears to vary from scene to scene. Zooming into known fire areas, we see that high CIBR values follow the outline of the fire front (Figure 7, bottom row). The CO_2 CIBR quantifies the proportion of emitted radiation in the measured spectral radiance value at a specific wavelength. To make it more useful standing on its own the image would have to be de-striped and cloud-masked, which would come at the cost of losing further detail in the signal.

An average of 18 HFDI band combination produces crisp fire maps with HFDI values that appear to correlate with fire intensities. Averaging helps reduce the noise inherent in Hyperion data. The Hyperion-specific averaged HFDI provided a reasonably stable detection threshold that did not vary greatly between three fire events in the Alaska boreal forest. A downside of band-averaging is that it effectively lowers the spectral resolution of the imaging spectrometry data, from 10 nm to 60 nm (six shorter-wavelength bands) and 30 nm (three longer-wavelength bands). Even a 60 nm bandwidth is still relatively small compared to common satellite-borne multispectral sensors (for example Landsat 8 OLI SWIR band 7: 187 nm). Essentially, opting for a band-averaged index rather a than single-band index reflects a necessary choice to avoid noisy or sub-optimally located Hyperion bands. In general, a normalized-difference based index is likely to be less susceptible to spectral resolution than an index that relies on an individual spectral feature. Opportunities for better fire detection using the HFDI-type normalized detection indices will require improved performance of future sensors in the 2̃400 - 2500 nm range, beyond the end of Hyperion's range of calibrated channels, and reduced noise across the SWIR range, rather than a finer spectral resolution.

Dennison and Roberts (2009) indicate that an HFDI-type index does not increase monotonically with fire intensity for very hot fires (T >1400 K), for which the emitted radiance at the shorter wavelength (approximately 2060 nm) will begin to exceed the radiance at the longer wavelength (approximately 2400 nm). For Hyperion, however, we do not find non-saturated pixels with usable data in this temperature range and can therefore assume that for our data, higher HFDI values correspond to higher fire intensities. The HFDI values found in the Crazy and Boundary fire data appear to be consistent with this principle (Figure 7): The HFDI reveals rich fire intensity patterns, which are an improvement over the result we obtained from supervised classification. A mixed approach that relies on all 18 HFDI band combinations plus the CO_2 CIBR was able to achieve a small improvement in classification accuracy, but at the cost of losing a single meaningful scalar index.

The linear spectral mixture analysis yields an overall excellent result for retrieving active fire temperatures based on two constant background components (vegetation and fire scar) and two active fire components whose temperatures were allowed to vary freely from pixel to pixel. Measured spectra with very small fractional areas (< 1%, that is, 5 - 9 m^2) of high-temperature active fire on a mixed vegetation and fire scar background were fitted extremely well (Figure 8d). The same is true for pixels that contain a somewhat larger fractional area of low-temperature fire (Figure 8e). Even pixels with 20 % to 25 % (approximately 200 m^2) of high-intensity active fire (Figure 8e) were modeled quite well even though the Hyperion sensor saturates in the SWIR region at such signal intensities. Typical temperatures for high-temperature fire components ranged from 800 K to 900 K. This value, which is not very high for wildfire, is limited by the saturation behavior of the Hyperion sensor: Beyond 900 K, the spectral radiance contribution in the longer-wavelength part of the SWIR region (>1900 nm) saturates the sensor; a meaningful temperature retrieval becomes impossible. The low temperatures of fire components were typically at values of 500 K to 600 K, which falls within the region of smoldering combustion of organic forest soil matter (Rein et al., 2008). The model therefore provides a pixel-by-pixel characterization of fire behavior properties. We were able to map hotter and cooler fire areas, and regions in which active fire occupies a larger or smaller fractional pixel area (Figure 9).

There are two limitations for temperature retrieval in our study: First, pixels with severe SWIR data anomalies such as drop-outs and some saturation behavior cannot be fitted well (Figure 8b). Second, some fire pixels are dominated by a reflected radiance component that exceeds the typical vegetation-type background at the shorter-wavelength end (1400 -

1800 nm). These pixels contain a source of reflected solar radiation that was not adequately captured by our choice of an averaged vegetation background spectrum (Figure 8c). Due to the small size of the study area (and the narrowness of the Hyperion swath) we considered it sufficient to use per-scene constant vegetation and fire scar endmembers; the unsatisfactory fit of some pixels highlights the limitation of this assumption. We could overcome it by applying a contextual selection and averaging mechanism to determine pixel-by-pixel background contributions. Such background contributions should continue to further distinguish between fire scar and vegetation and would provide improved information on the fractional areas of a pixel that are unburned versus already-burned.

7. Conclusions, recommendations, and future work

We have demonstrated the usefulness of a Hyperion-type hyperspectral sensor to detect, map, and characterize active fire in Alaska's boreal forest as well as the land cover changes introduced by fire (fire scar and unburned vegetation). We detected both high-intensity flaming fire and low-temperature combustion likely associated with smoldering fire. Sensors like Hyperion have great potential to further identify classes of fuel type (Dennison et al., 2006) and condition, as well as the properties of both fresh and older burn scars. One area for future research includes fire severity, which, in the Alaska boreal forest, is associated with the degree to which the sub- surface layers of organic matter are consumed (Lentile et al., 2006). Such work requires a field component.

Future instruments are already being designed with an emphasis on enhanced SNR, as is the case for HyspIRI at 500:1 (2200 nm) (Lee et al., 2015), PRISMA at >200:1 (VNIR and SWIR) (Labate et al., 2009), and EnMAP at >150:1 (SWIR) (Kaufmann et al., 2006), compared to Hyperion's SNR of 38:1 at 2125 nm (Pearlman et al., 2003). Areas of active combustion represent a larger percentage of total pixel area as spatial resolution is increased, so finer spatial resolutions could make the detection of weak spectral features, such as the K-emission line, more likely. Such a requirement, though, is in conflict with a shorter repeat interval, which would be highly desirable for monitoring relatively rapid landscape processes such as a change in pre-fire fuel conditions or fire effects. Similarly, improved saturation behavior needs to be considered as a trade-off with sensor sensitivity (Realmuto et al., 2015). Design goals such as a short recovery lag before saturated sensor elements are operational again or a well-documented signature of sensor saturation are likely to be preferable to a high saturation threshold on a sensor that is incapable of picking up weak heat signals.

We hope that new and enhanced satellite-borne imaging spectrometers will become available in order to expand our ability to understand active wildfire in its biophysical context. As our work showed, spectral bands from the atmospheric windows of the SWIR portion of the electromagnetic spectrum (combining both the 1500-1800 nm and the 2000-2500 nm range) are suitable to detect active fire, characterize it (T-retrieval), and classify the pre- and post-fire land cover. Our research demonstrated a repeatable process to define a modified HFDI using specific ranges of spectral bands, which, either alone or in combination with the CIBR, resulted in high-quality detection of active fire. Future instruments would enhance the investigation of climate and environmental change, the carbon cycle, and, ultimately, might even open new avenues for operational fire monitoring

8. Acknowledgements

This research was supported by NASA Headquarters under the NASA Earth and Space Science Fellowship Program – Grant NNX13AN90H. This publication is the result in part of research sponsored by the Cooperative Institute for Alaska Research with funds from the National Oceanic and Atmospheric Administration under cooperative agreement NA13OAR4320056 with the University of Alaska. The authors acknowledge support from Alaska EPSCoR NSF award #OIA-1208927 and the state of Alaska. We are thankful for the support of the Alaska Climate Research Center.

The authors thank the United States Geological Survey for Hyperion data, the University of Wyoming Atmospheric Sciences Department for the radiosonde data and BLM/Alaska Fire Service for fire perimeter data used in Figure 1.

The open-source scientific Python libraries scikit-learn (Pedregosa et al., 2011) and scipy (Jones et al., 2001–) were used for Random Forest classification and curve fitting.

References

Abrams, M., Pieri, D., Realmuto, V., Wright, R., 2013. Using EO-1 Hyperion Data as HyspIRI Preparatory Data Sets for Volcanology Applied to Mt Etna, Italy. IEEE Journal of Selected Topics in Applied Earth Observations and Remote Sensing 6, 375–385. URL: http://dx.doi.org/10.1109/JSTARS.2012.2224095.

AICC, 2004. Alaska Fire Season 2004. Technical Report. Alaska Interagency Coordination Center. URL: https://fire.ak.blm.gov/content/aicc/Statistics%20Directory/Previous%20Years%20Fall%20Fire%20Review%20Handouts/Yearly%20Fire%20Statistics%20Archive/2004.pdf.

AICC, 2009. Alaska Fire Season 2009: Wildland Fire Summary and Statistics Annual Report. Technical Report. Alaska Interagency Coordination Center. URL: https://fire.ak.blm.gov/content/aicc/Statistics%20Directory/Previous%20Years%20Fall%20Fire%20Review%20Handouts/Yearly%20Fire%20Statistics%20Archive/2009.pdf.

Amici, S., Wooster, M.J., Piscini, A., 2011. Multi-resolution spectral analysis of wildfire potassium emission signatures using laboratory, airborne and spaceborne remote sensing. Remote Sensing of Environment 115, 1811–1823. URL: http://dx.doi.org/10.1016/j.rse.2011.02.022.

Barry, P., 2001. EO-1/Hyperion science data user's guide, Level 1_B. TRW Space, Defense & Information Systems, Redondo Beach, CA. URL: https://eo1.gsfc.nasa.gov/new/general/Disk2/HyperionScienceDataUsersGuide_public_L1B.pdf.

Ben Dor, E., Kafri, A., Varacalli, G., 2014. SHALOM: An Italian–Israeli hyperspectral orbital mission: Update, in: International Geoscience and Remote Sensing Symposium, Quebec, Canada, July 13–18, 2014.

Berk, A., Anderson, G.P., Acharya, P.K., Bernstein, L.S., Muratov, L., Lee, J., Fox, M., Adler-Golden, S.M., Chetwynd, J.H., Hoke, M.L., Lockwood, R.B., Gardner, J.A., Cooley, T.W., Borel, C.C., Lewis, P.E., Shettle, E.P., 2006. MODTRAN5: 2006 update, International Society for Optics and Photonics. p. 62331F. URL: https://www.spiedigitallibrary.org/conference-proceedings-of-spie/6233/62331F/MODTRAN5-2006-update/10.1117/12.665077.short.

Breiman, L., 2001. Random Forests. Machine Learning 45, 5–32. URL: http://dx.doi.org/10.1023/A:1010933404324.

Briess, K., Jahn, H., Lorenz, E., Oertel, D., Skrbek, W., Zhukov, B., 2003. Fire recognition potential of the bi-spectral Infrared Detection (BIRD) satellite. International Journal of Remote Sensing 24, 865–872. URL: http://dx.doi.org/10.1080/01431160210154010.

Cahill, C.F., Cahill, T.A., Perry, K.D., 2008. The size- and time-resolved composition of aerosols from a sub-Arctic boreal forest prescribed burn. Atmospheric Environment 42, 7553–7559. URL: http://dx.doi.org/10.1016/j.atmosenv.2008.04.034.

Calef, M.P., Varvak, A., McGuire, A.D., Chapin, F.S., Reinhold, K.B., 2015. Recent Changes in Annual Area Burned in Interior Alaska: The Impact of Fire Management. Earth Interactions 19, 1–17. URL: http://dx.doi.org/10.1175/EI-D-14-0025.1.

Chapin, F.S., McGuire, A.D., Randerson, J., Pielke, R., Baldocchi, D., Hobbie, S.E., Roulet, N., Eugster, W., Kasischke, E., Rastetter, E.B., Zimov, S.A., Running, S.W., 2000. Arctic and boreal ecosystems of western North America as components of the climate system. Global Change Biology 6, 211–223. URL: http://dx.doi.org/10.1046/j.1365-2486.2000.06022.x.

Dalponte, M., Ørka, H.O., Gobakken, T., Gianelle, D., Næsset, E., 2013. Tree Species Classification in Boreal Forests With Hyperspectral Data. IEEE Transactions on Geoscience and Remote Sensing 51, 2632–2645. URL: http://dx.doi.org/10.1109/TGRS.2012.2216272.

Dennison, P.E., 2006. Fire detection in imaging spectrometer data using atmospheric carbon dioxide absorption. International Journal of Remote Sensing 27, 3049–3055. URL: http://dx.doi.org/10.1080/01431160600660871.

Dennison, P.E., Charoensiri, K., Roberts, D.A., Peterson, S.H., Green, R.O., 2006. Wildfire temperature and land cover modeling using hyperspectral data. Remote Sensing of Environment 100, 212–222. URL: http://dx.doi.org/10.1016/j.rse.2005.10.007.

Dennison, P.E., Matheson, D.S., 2011. Comparison of fire temperature and fractional area modeled from SWIR, MIR, and TIR multispectral and SWIR hyperspectral airborne data. Remote Sensing of Environment 115, 876–886. URL: http://dx.doi.org/10.1016/j.rse.2010.11.015.

Dennison, P.E., Roberts, D.A., 2009. Daytime fire detection using airborne hyperspectral data. Remote Sensing of Environment 113, 1646–1657. URL: http://dx.doi.org/10.1016/j.rse.2009.03.010.

Dozier, J., 1981. A method for satellite identification of surface temperature fields of subpixel resolution. Remote Sensing of Environment 11, 221–229. URL: http://dx.doi.org/10.1016/0034-4257(81)90021-3.

Feingersh, T., Ben Dor, E., 2015. SHALOM–a commercial hyperspectral space mission , 247.

Flannigan, M.D., Haar, T.H.V., 1986. Forest fire monitoring using NOAA satellite AVHRR. Canadian Journal of Forest Research 16, 975–982. URL: http://dx.doi.org/10.1139/x86-171.

Friedman, J., Hastie, T., Tibshirani, R., 2001. Chapter 7: Model assessment and selection, in: The Elements of Statistical Learning. Springer Series in Statistics, Springer, Berlin. volume 1. URL: http://statweb.stanford.edu/~tibs/book/preface.ps.

Giglio, L., Csiszar, I., Restás, A., Morisette, J.T., Schroeder, W., Morton, D., Justice, C.O., 2008. Active fire detection and characterization with the advanced spaceborne thermal emission and reflection radiometer (ASTER). Remote Sensing of Environment 112, 3055–3063. URL: http://dx.doi.org/10.1016/j.rse.2008.03.003.

Giglio, L., Descloitres, J., Justice, C.O., Kaufman, Y.J., 2003. An Enhanced Contextual Fire Detection Algorithm for MODIS. Remote Sensing of Environment 87, 273–282. URL: http://dx.doi.org/10.1016/S0034-4257(03)00184-6.

Giglio, L., Kendall, J.D., 2001. Application of the Dozier retrieval to wildfire characterization: a sensitivity analysis. Remote Sensing of Environment 77, 34–49. URL: http://dx.doi.org/10.1016/S0034-4257(01)00192-4.

Giglio, L., Randerson, J.T., van der Werf, G.R., 2013. Analysis of daily, monthly, and annual burned area using the fourth-generation global fire emissions database (GFED4). Journal of Geophysical Research: Biogeosciences 118, 317–328. URL: http://dx.doi.org/10.1002/jgrg.20042.

Giglio, L., Schroeder, W., Justice, C.O., 2016. The collection 6 MODIS active fire detection algorithm and fire products. Remote Sensing of Environment 178, 31–41. URL: http://dx.doi.org/10.1016/j.rse.2016.02.054.

Goodenough, D., Dyk, A., Niemann, K., Pearlman, J., Chen, H., Han, T., Murdoch, M., West, C., 2003. Processing Hyperion and ALI for forest classification. IEEE Transactions on Geoscience and Remote Sensing 41, 1321–1331. URL: http://dx.doi.org/10.1109/TGRS.2003.813214.

Grell, G., Freitas, S.R., Stuefer, M., Fast, J., 2011. Inclusion of biomass burning in WRF-Chem: impact of wildfires on weather forecasts. Atmos. Chem. Phys. 11, 5289–5303. URL: http://dx.doi.org/10.5194/acp-11-5289-2011.

Ham, J., Chen, Y., Crawford, M.M., Ghosh, J., 2005. Investigation of the random forest framework for classification of hyperspectral data. IEEE Transactions on Geoscience and Remote Sensing 43, 492–501. URL: http://dx.doi.org/10.1109/TGRS.2004.842481.

Ichoku, C., Kahn, R., Chin, M., 2012. Satellite contributions to the quantitative characterization of biomass burning for climate modeling. Atmospheric Research 111, 1–28. URL: http://dx.doi.org/10.1016/j.atmosres.2012.03.007.

Jia, G.J., Burke, I.C., Kaufmann, M.R., Goetz, A.F., Kindel, B.C., Pu, Y., 2006. Estimates of forest canopy fuel attributes using hyperspectral data. Forest Ecology and Management 229, 27–38. URL: http://dx.doi.org/10.1016/j.foreco.2006.03.021.

Johnstone, J.F., Hollingsworth, T.N., Chapin, F.S., Mack, M.C., 2010. Changes in fire regime break the legacy lock on successional trajectories in Alaskan boreal forest. Global Change Biology 16, 1281–1295. URL: http://dx.doi.org/10.1111/j.1365-2486.2009.02051.x.

Jones, E., Oliphant, T., Peterson, P., et al., 2001–. SciPy: Open source scientific tools for Python. URL: http://www.scipy.org/. [Online; accessed 2017-09-11].

Kasischke, E.S., Verbyla, D.L., Rupp, T.S., McGuire, A.D., Murphy, K.A., Jandt, R., Barnes, J.L., Hoy, E.E., Duffy, P.A., Calef, M., Turetsky, M.R., 2010. Alaska's changing fire regime — implications for the vulnerability of its boreal forests. Canadian Journal of Forest Research 40, 1313–1324. URL: http://dx.doi.org/10.1139/X10-098.

Kasischke, E.S., Williams, D., Barry, D., 2002. Analysis of the patterns of large fires in the boreal forest region of Alaska. Int. J. Wildland Fire 11, 131–144. URL: http://www.publish.csiro.au/paper/WF02023.

Kaufman, Y.J., Justice, C.O., Flynn, L.P., Kendall, J.D., Prins, E.M., Giglio, L., Ward, D.E., Menzel, W.P., Setzer, A.W., 1998. Potential global fire monitoring from EOS-MODIS. Journal of Geophysical Research 103, PP. 32,215–32,238. URL: http://dx.doi.org/199810.1029/98JD01644.

Kaufmann, H., Segl, K., Chabrillat, S., Hofer, S., Stuffler, T., Mueller, A., Richter, R., Schreier, G., Haydn, R., Bach, H., 2006. EnMAP A Hyperspectral Sensor for Environmental

Mapping and Analysis, in: 2006 IEEE International Symposium on Geoscience and Remote Sensing, pp. 1617–1619. URL: http://dx.doi.org/10.1109/IGARSS.2006.417.

Kerola, D.X., Bruegge, C.J., Gross, H.N., Helmlinger, M.C., 2009. On-orbit calibration of the EO-1 Hyperion and Advanced Land Imager (ALI) sensors using the LED Spectrometer (LSpec) automated facility 47, 1244–1255. doi:10.1109/TGRS.2008.2008904.

Labate, D., Ceccherini, M., Cisbani, A., De Cosmo, V., Galeazzi, C., Giunti, L., Melozzi, M., Pieraccini, S., Stagi, M., 2009. The PRISMA payload optomechanical design, a high performance instrument for a new hyperspectral mission. Acta Astronautica 65, 1429–1436. URL: http://dx.doi.org/10.1016/j.actaastro.2009.03.077.

Lee, C.M., Cable, M.L., Hook, S.J., Green, R.O., Ustin, S.L., Mandl, D.J., Middleton, E.M., 2015. An introduction to the NASA Hyperspectral InfraRed Imager (HyspIRI) mission and preparatory activities. Remote Sensing of Environment 167, 6–19. URL: http://dx.doi.org/10.1016/j.rse.2015.06.012.

Lentile, L.B., Holden, Z.A., Smith, A.M.S., Falkowski, M.J., Hudak, A.T., Morgan, P., Lewis, S.A., Gessler, P.E., Benson, N.C., 2006. Remote sensing techniques to assess active fire characteristics and post-fire effects. International Journal of Wildland Fire 15, 319–345. URL: http://dx.doi.org/10.1071/WF05097.

Lewis, S.A., Hudak, A.T., Ottmar, R.D., Robichaud, P.R., Lentile, L.B., Hood, S.M., Cronan, J.B., Morgan, P., 2011. Using hyperspectral imagery to estimate forest floor consumption from wildfire in boreal forests of Alaska, USA. International Journal of Wildland Fire 20, 255–271. URL: http://dx.doi.org/10.1071/WF09081.

Middleton, E., Campbell, P.K.E., Ungar, S., Ong, L., Zhang, Q., Huemmrich, K., Mandl, D., Frye, S., 2010. Using EO-1 Hyperion images to prototype environmental products for HyspIRI, in: Geoscience and Remote Sensing Symposium (IGARSS), 2010 IEEE International, pp. 4256–4259. URL: http://dx.doi.org/10.1109/IGARSS.2010.5648946.

Middleton, E., Ungar, S., Mandl, D., Ong, L., Frye, S., Campbell, P., Landis, D., Young, J., Pollack, N., 2013. The Earth Observing One (EO-1) Satellite Mission: Over a Decade in Space. IEEE Journal of Selected Topics in Applied Earth Observations and Remote Sensing 6, 243–256. URL: http://dx.doi.org/10.1109/JSTARS.2013.2249496.

Pearlman, J., Barry, P., Segal, C., Shepanski, J., Beiso, D., Carman, S., 2003. Hyperion, a space-based imaging spectrometer. IEEE Transactions on Geoscience and Remote Sensing 41, 1160–1173. URL: http://dx.doi.org/10.1109/TGRS.2003.815018.

Pedregosa, F., Varoquaux, G., Gramfort, A., Michel, V., Thirion, B., Grisel, O., Blondel, M., Prettenhofer, P., Weiss, R., Dubourg, V., Vanderplas, J., Passos, A., Cournapeau, D., Brucher, M., Perrot, M., Duchesnay, E., 2011. Scikit-learn: Machine Learning in Python. Journal of Machine Learning Research 12, 2825–2830. URL: http://jmlr.csail.mit.edu/papers/v12/pedregosa11a.html.

Prakash, A., Schaefer, K., Witte, W.K., Collins, K., Gens, R., Goyette, M.P., 2011. A Remote Sensing and GIS Based Investigation of a Boreal Forest Coal Fire. International Journal of Coal Geology 86, 79–86. URL: http://dx.doi.org/10.1016/j.coal.2010.12.001.

Randerson, J.T., Liu, H., Flanner, M.G., Chambers, S.D., Jin, Y., Hess, P.G., Pfister, G., Mack, M.C., Treseder, K.K., Welp, L.R., Chapin, F.S., Harden, J.W., Goulden, M.L., Lyons, E., Neff, J.C., Schuur, E.a.G., Zender, C.S., 2006. The Impact of Boreal Forest Fire on Climate Warming. Science 314, 1130–1132. URL: http://dx.doi.org/10.1126/science.1132075.

Realmuto, V.J., Dennison, P.E., Foote, M., Ramsey, M.S., Wooster, M.J., Wright, R., 2015. Specifying the saturation temperature for the HyspIRI 4-μm channel. Remote Sensing of Environment 167, 40–52. URL: http://dx.doi.org/10.1016/j.rse.2015.04.028.

Rein, G., Cleaver, N., Ashton, C., Pironi, P., Torero, J.L., 2008. The severity of smouldering peat fires and damage to the forest soil. CATENA 74, 304–309. URL: http://dx.doi.org/10.1016/j.catena.2008.05.008.

Roberts, D., Dennison, P., Gardner, M., Hetzel, Y., Ustin, S., Lee, C., 2003. Evaluation of the potential of Hyperion for fire danger assessment by comparison to the Airborne Visible/Infrared Imaging Spectrometer. IEEE Transactions on Geoscience and Remote Sensing 41, 1297–1310. URL: http://dx.doi.org/10.1109/TGRS.2003.812904.

Roberts, D.A., Gardner, M., Church, R., Ustin, S., Scheer, G., Green, R.O., 1998. Mapping chaparral in the Santa Monica Mountains using multiple endmember spectral mixture models. Remote Sensing of Environment 65, 267–279. URL: http://dx.doi.org/10.1016/S0034-4257(98)00037-6.

Roberts, D.A., Quattrochi, D.A., Hulley, G.C., Hook, S.J., Green, R.O., 2012. Synergies between VSWIR and TIR data for the urban environment: An evaluation of the potential for the Hyperspectral Infrared Imager (HyspIRI) Decadal Survey mission. Remote Sensing of Environment 117, 83–101. URL: http://dx.doi.org/10.1016/j.rse.2011.07.021.

Robinson, J.M., 1991. Fire from space: Global fire evaluation using infrared remote sensing. International Journal of Remote Sensing 12, 3–24. URL: http://dx.doi.org/10.1080/01431169108929628.

Rogass, C., Mielke, C., Scheffler, D., Boesche, N., Lausch, A., Lubitz, C., Brell, M., Spengler, D., Eisele, A., Segl, K., Guanter, L., 2014. Reduction of uncorrelated striping noise—applications for hyperspectral pushbroom acquisitions 6, 11082–11106. URL: http://www.mdpi.com/2072-4292/6/11/11082, doi:10.3390/rs61111082.

Schroeder, W., Oliva, P., Giglio, L., Csiszar, I.A., 2014. The New VIIRS 375 m active fire detection data product: Algorithm description and initial assessment. Remote Sensing of Environment 143, 85–96. URL: http://dx.doi.org/10.1016/j.rse.2013.12.008.

Schroeder, W., Oliva, P., Giglio, L., Quayle, B., Lorenz, E., Morelli, F., 2015. Active fire detection using Landsat-8/OLI data. Remote Sensing of Environment URL: http://dx.doi.org/10.1016/j.rse.2015.08.032.

Simon, K., 2006. Hyperion Level 1GST (L1GST) Product Output Files Data Format Control Book (DFCB). Technical Report EO1-DFCB-0003. Department of the Interior US Geological Survey.

Ungar, S., Pearlman, J., Mendenhall, J., Reuter, D., 2003. Overview of the Earth Observing One (EO-1) mission. IEEE Transactions on Geoscience and Remote Sensing 41, 1149–1159. URL: http://dx.doi.org/10.1109/TGRS.2003.815999.

Vodacek, A., Kremens, R.L., Fordham, A.J., Vangorden, S.C., Luisi, D., Schott, J.R., Latham, D.J., 2002. Remote optical detection of biomass burning using a potassium emission signature. International Journal of Remote Sensing 23, 2721–2726. URL: http://dx.doi.org/10.1080/01431160110109633.

Waigl, C.F., Stuefer, M., Prakash, A., Ichoku, C., 2017. Detecting high and low-intensity fires in Alaska using VIIRS I-band data: An improved operational approach for high latitudes 199, 389–400. URL: http://www.sciencedirect.com/science/article/pii/S0034425717303085, doi:10.1016/j.rse.2017.07.003.

Wendler, G., Conner, J., Moore, B., Shulski, M., Stuefer, M., 2010. Climatology of Alaskan wildfires with special emphasis on the extreme year of 2004. Theoretical and Applied Climatology 104, 459–472. URL: http://dx.doi.org/10.1007/s00704-010-0357-9.

Wright, R., Garbeil, H., Davies, A.G., 2010. Cooling rate of some active lavas determined using an orbital imaging spectrometer. Journal of Geophysical Research: Solid Earth (1978–2012) 115. URL: http://dx.doi.org/10.1029/2009JB006536.